A Numerical Study on the Bubble Noise and the Tip Vortex Cavitation Inception

Jin-Keun Choi[1] and Georges L. Chahine[1]

[1]DYNAFLOW, INC.; E-mail: jinkeun2000@hotmail.com

Abstract

This paper presents a numerical study on tip vortex cavitation inception predictions based on non-spherical bubble dynamics including splitting and jet noise emission. A brief summary of the numerical method and its validation against a laboratory experiment are presented. The behavior of bubble nuclei is studied in a tip vortex flow field at two Reynolds numbers, provided by a viscous flow solver. The bubble behavior is simulated by an axisymmetric potential flow solver with the effect of surrounding viscous flow taken into account using one way coupling. The effects of bubble nucleus size and Reynolds number are studied. An effort to model the bubble splitting at lower cavitation numbers is also described.

Keywords: bubble dynamics, tip vortex, cavitation inception, cavitation noise, boundary element method

Nomenclature

k	exponent of the polytropic gas low
n	coordinate normal to the bubble surface
p	pressure
p_g	gas pressure
$p_{g,B}$	gas pressure just before the split
$p_{g,o}$	initial gas pressure
p_ω	pressure in the pre-existing vortex field
Re	Reynolds number, $Re = U_\infty L_{chord}/\nu$
R_o	initial radius of the bubble
t	time
$\mathbf{u}_{total}$	total velocity, $\mathbf{u}_{total} = \mathbf{u} + \mathbf{v}$
$\mathbf{u}$	potential flow velocity, $\mathbf{u} = \nabla\phi$
$\mathbf{v}$	rotational flow velocity
$\mathcal{V}$	bubble volume
$\mathcal{V}_A, \mathcal{V}_B$	bubble volume just after, before the split
$\mathcal{V}_i$	volume of the i-th bubble after splitting
$\mathcal{V}_o$	initial bubble volume
ϕ	velocity potential

σ cavitation number, $\sigma = (p - p_v) / \left(\frac{1}{2}\rho U_\infty^2\right)$

σ_i cavitation inception number

1 Introduction

Recently, successful numerical approaches to the prediction of tip vortex cavitation inception and its scaling have been developed by coupling bubble dynamics models and unsteady Reynolds Averaged Navier Stokes (RANS) equation methods (Hsiao and Chahine 2002, Hsiao et al 2003). In such approaches, both spherical bubbles dynamics models (modified Rayleigh-Plesset equation) and non-spherical bubble models (boundary element methods) have been utilized in handling the bubble dynamics part of the coupling. It has been found that each model used in the coupling has its own merits and drawbacks. The spherical model can describe many growth and collapse cycles producing high pressure peaks at each rebound, but is limited to spherical bubble geometries. On the other hand, the non-spherical model can more correctly simulate bubble deformation (Chahine 1995), but has difficulty providing the pressure peaks because the numerical method usually becomes very unstable near the first collapse of the bubble.

In an effort to extend the capabilities of the non-spherical method, we have developed a non-spherical axisymmetric method that can simulate the extreme bubble deformations including bubble splitting and following cyclic behavior (Choi and Chahine 2002). When the method is applied to a bubble in a tip vortex flow field, it is found that the bubble elongates in the vortex field and, under certain conditions, splits at the end of the elongation, after which violent reentrant jets develop from the split. It is also found that such splitting and reentrant jet formation are accompanied with strong pressure pulse emission, which are one or two orders of magnitude higher than those obtained by the spherical bubble model. This finding could be of practical importance since tip vortex cavitation inception is more often detected acoustically than visually.

The interactive dynamics of bubbles and surrounding vortices can be categorized into three phases; (a) the bubble capture by the vortex, (b) the interaction between the vortex and an initially quasi-spherical bubble on its axis, and (c) the dynamics of elongated bubbles on the vortex axis. In this study, the last phase of the dynamics is of main interest and the utilization of an axisymmetric method can be justified. The axisymmetric code, 2DYNAFS©, has been verified successfully for diverse types of fluid dynamic problems in the past (Chahine et al 1996). Recently, the code has been extended to accommodate the ambient vortex flow field and to model the extreme deformation of the bubble including splitting (Choi and Chahine 2002, Choi and Chahine 2003).

There are a few investigations (Chahine 1982, Kucherenko and Shamko 1986, Ishida et al 2001) on the bubble splitting behavior between two parallel plates in the past. They showed the hourglass-like bubble deformation through experiments and theoretical predictions. Ishida et al (2001) reported the existence of a small peak in the pressure signal at the splitting of the bubble. However, none of them were able to simulate the bubble behavior beyond the spitting nor to predict the pressure signal from such extreme bubble behaviors.

In this paper, we present a numerical study on tip vortex cavitation inception predictions based on bubble splitting and jet noise emission. A brief summary of the numerical method and its validation against a laboratory experiment are presented. For the numerical studies, the tip vortex flow fields of an elliptic hydrofoil at two Reynolds numbers are provided by a viscous flow solver. The bubble behavior is simulated by the axisymmetric potential flow solver with the effect of surrounding viscous flow taken into account by the so called one way coupling. The effect of

bubble nucleus size and the effect of Reynolds number are studied. An effort to model the bubble splitting at lower cavitation numbers is also described.

2 Numerical methods

For a general description of the bubble deformation in a vortex field, the non-spherical bubble geometry should be modeled. In the present study, an axisymmetric formulation is used to take advantage of the axisymmetric vortex field. Under the assumption of axisymmetry, only the bubble behavior after the bubble has reached the vortex axis is possible. For practical predictions, the spherical model can be used during the capture of the bubble because the bubble remains practically spherical until it reaches the vortex axis. A more general alternative approach is a fully three-dimensional method that has been used in our other studies (Hsiao and Chahine 2002).

To be able to consider the ambient viscous flow field inside the vortex core, we base our approach on the Helmholtz decomposition. That is, any velocity field can be expressed by the sum of the gradient of a scalar potential and the rotational flow field.

$$\mathbf{u}_{total} = \mathbf{u} + \mathbf{v} = \nabla \phi + \mathbf{v} \tag{1}$$

The perturbed flow field due to the bubble presence is assumed to be expressed by $\mathbf{u} = \nabla \phi$ and the rotational flow field $\mathbf{v}$ of the tip vortex flow is assumed to remain not affected by the bubble presence and its dynamics (Chahine et al 1997). Since the potential flow field due to the bubble presence satisfies the Laplace equation $\nabla^2 \phi = 0$, Green's identity can be applied to construct the integral equation for the potential ϕ and the normal derivative of the potential $\partial \phi / \partial n$.

The boundary conditions on the bubble surface are the continuity of the normal stresses (the dynamic condition) and the condition that the fluid normal velocities should be equal to the interface normal velocities (the kinematic condition). On the bubble surface, $\partial \phi / \partial n$ is obtained as the solution of the integral equation, while ϕ is given from the dynamic boundary condition through the Euler time stepping scheme. In order to find an expression for $\partial \phi / \partial t$ on the bubble surface, $\mathbf{u}_{total}$ of the Helmholtz decomposition (1) is substituted into the Navier-Stokes equation. Under the assumption that the pre-existing vortex field satisfies the Navier-Stokes equation, the resulting equation simplifies to the modified Bernoulli's equation,

$$\nabla \left\{ \frac{p - p_\omega}{\rho} + \frac{\partial \phi}{\partial t} + \frac{1}{2} |\nabla \phi|^2 + \mathbf{v} \cdot \nabla \phi \right\} = \nabla \phi \times (\nabla \times \mathbf{v}) \tag{2}$$

In the present study, the vorticity in the vortex field is further assumed to be predominant only in the axial direction.

The pressure inside each bubble is assumed homogeneous, and the gas inside each bubble is assumed to be composed of both vapor of the liquid and non-condensable gas. The pressure at any instant is given by the sum of the partial pressures of the liquid vapor and of the non-condensable gas. Vaporization of the liquid is assumed to occur at a fast enough rate so that the vapor pressure inside the bubble remains equal to the equilibrium liquid vapor pressure at the ambient temperature. The non-condensable gas is assumed to satisfy a polytropic gas law with the exponent k, and thus $p\mathcal{V}^k$ remains constant through the variation of the bubble volume $\mathcal{V}(t)$ with time. The pressure on the liquid side of the gas-liquid interface and the pressure inside the bubble are balanced by the surface tension that depends on the local curvature of the interface. Finally, the
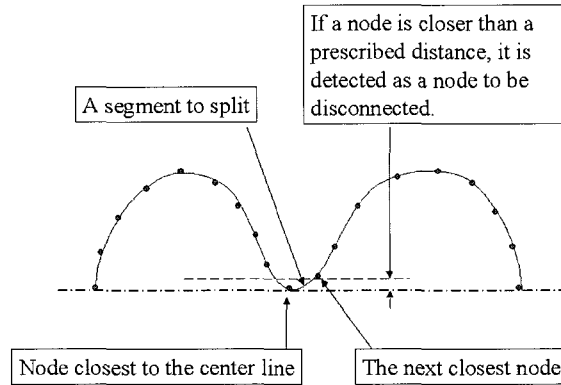
Figure 1: Schematic view of a bubble that splits into two sub-bubbles

Euler scheme based on the $\partial\phi/\partial t$ from the modified Bernoulli's equation (2) is applied to march the potential ϕ through the discretized time steps.

The bubble surface is discretized by straight line segments on a meridian plane. The potential is assumed to vary linearly over each segment, while the normal gradient of the potential is assumed constant over each segment. The integral equation is then collocated at the center of each segment, and the resulting matrix equation is solved by using a standard LU-decomposition technique. The normal velocity is known from the solution of the integral equation while the tangential velocity is obtained by numerical differentiation of the potential along the bubble surface. The new bubble geometry is obtained by advancing each node according to the sum of this local velocity and the velocity of the ambient vortex field. The time step size is controlled by an adaptive scheme that ensures that smaller time steps are chosen when the potential changes rapidly. Once the solution is obtained at any time step, the pressure signals at given field points can be calculated by using the Green identity and the unsteady Bernoulli equation. First, the Green identity is used to calculate the potential at given field points, and then the velocity is obtained from numerical differentiation. Finally, the pressure can be calculated by the Bernoulli equation.

A bubble placed on the vortex axis usually elongates along this axis. Oftentimes the elongation is so extreme that the bubble eventually splits into smaller sub-bubbles. When this happens, a special treatment is necessary to continue the simulation. A schematic view of a bubble about to split is shown in Figure 1. When a node approaches the axis within a specified small distance, three nodes including two neighboring nodes are tested to find the two nodes that are closest to the axis. The segment connecting these two nodes is detected as the segment to split. This detection procedure can be complex if multiple nodes approach the axis simultaneously or the bubble splits into more than three sub-bubbles at the same time step. Once a segment to split is found, the segment is removed by placing the two end nodes of the segment exactly on the axis. Many variables including potential and velocities need to be extrapolated to the new position and the node and segment indices as well as the bubble index are updated. In the present study, the gas pressure is kept constant through the splitting. Alternatively, one could prescribe a given pressure loss during the splitting. The gas pressure before the split can be expressed as $p_{g,B} = p_{g,o}\left(\mathcal{V}_o/\mathcal{V}_B\right)^k$, where the subscript B represents the quantity just before the splitting. Then the
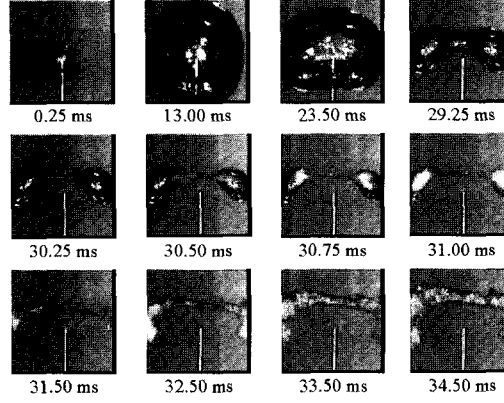
Figure 2: Behavior of a bubble generated by a spark between two vertical plates. The time under each image is the time from the moment of the spark. Two vertical plates are placed just outside of the view. The second electrode cannot be shown because it is exactly behind the one shown in the images
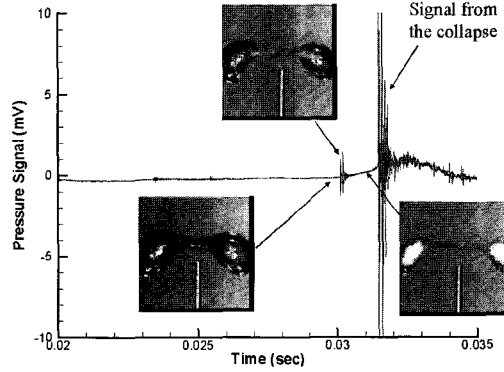

Figure 3: Measured pressure signal from the bubble splitting between two vertical plates

gas pressure after the splitting can be calculated by

$$p_g\left(t\right) = p_{g,B}\left\{\frac{\mathcal{V}_{i,A}}{\mathcal{V}_i\left(t\right)}\right\}^k = p_{g,o}\left\{\frac{\mathcal{V}_o}{\mathcal{V}_B}\right\}^k\left\{\frac{\mathcal{V}_{i,A}}{\mathcal{V}_i\left(t\right)}\right\}^k \tag{3}$$

where $\mathcal{V}_{i,A}$ is the volume of the i-th sub-bubble just after the splitting and $\mathcal{V}_i\left(t\right)$ is the volume of the i-th sub-bubble at arbitrary later time t. The sum of $\mathcal{V}_{i,A}$ over all sub-bubbles should be equal to $\mathcal{V}_B$, unless the process involves loss of gas, which is not considered in the present study.

3 Bubble splitting experiment

A preliminary experiment is performed to observe the behavior of the bubble at its splitting and to investigate if any noise signal is present at the splitting. A usual difficulty in studying the splitting noise experimentally is to obtain a separate signal of the splitting because the splitting is very closely followed by the collapse of the sub-bubbles with violent pressure pulses. Our experiment is carefully designed so that the two signals are separated as much as possible.
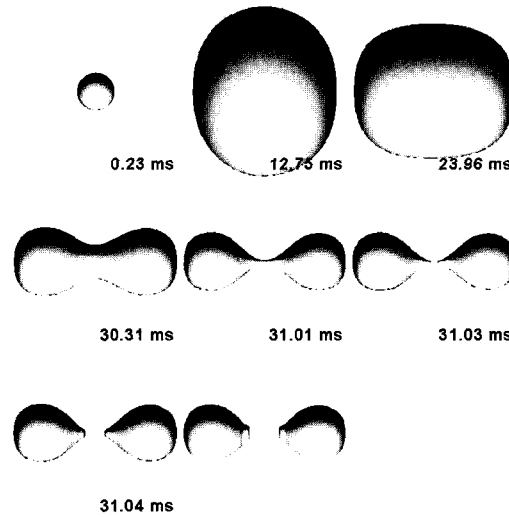
17

Figure 4: Simulated bubble behavior between the two vertical plates predicted by the axisymmetric method, 2DYNAFS©

The bubble is generated by an electric spark from two electrodes submerged under water in a depressurized chamber. In order to induce the bubble to split, flat plates are placed near the spark generated bubble. Two vertical plates are spaced by 2 *in.* and two electrodes are placed right in the middle between the two plates. The ambient pressure at the level of the bubble center is 6000 *Pa*. Two sets of coaxial electrodes, each of which is charged with 10 *kV*, are used to generate the spark. A hydrophone is located at the same level of the bubble between the two plates. The video images (4000 frames per second) of the bubble behavior and the noise signal from the hydrophone are recorded simultaneously by a MIDAS software on a personal computer. Figure 2 shows the overall bubble behavior with more images very near the splitting moment.

The bubble generated from the spark starts to grow spherically in the beginning. As the bubble volume increases, its growth in the horizontal direction is restricted by the two vertical plates. After reaching its maximum volume, the bubble shrinks with a more rapid pace in the middle than near the two vertical plates. This is also the moment when the effect of gravity begins to show more clearly in the bubble shape. The bubble finally splits into two sub-bubbles, which collapse and break into many micro-bubbles later. At the split, the sub-bubbles seem to develop jets into themselves from the splitting. In Figure 3, the measured pressure signal near the bubble splitting and collapse is shown. Before the strong signal from the collapse of each of the sub-bubbles is observed, a smaller signal is captured at the moment of splitting.

A numerical simulation for the same case of the bubble between two vertical plates was performed by using 2DYNAFS©. Due to the axisymmetric assumption of the method, the gravity acting in the transverse (vertical) direction cannot be modeled in this numerical computation. The simulated bubble behavior shown in Figure 4 generally agrees with the video images of Figure 2. The numerical simulation stops when each jet touches the other side of each sub-bubble. It is interesting that the development of the jets in the two sub-bubbles after the split is very clearly shown in this simulation.

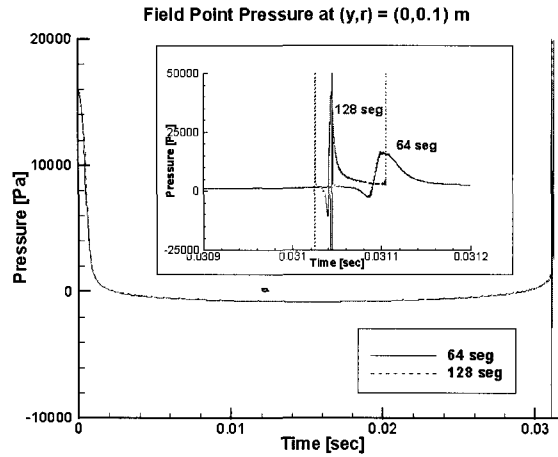The predicted pressure signal at the hydrophone location is shown in Figure 5. The predicted

Figure 5: Predicted pressure signals for the bubble between two vertical plates as simulated by the axisymmetric method, 2DYNAFS©. Results from the simulations with 64 segments and 128 segments are compared

pressure signals show a spike followed by an N-shaped pulse. The first spike exactly corresponds to the moment of splitting in the numerical simulation, and the N-shaped pulse corresponds to the forming of the reentrant jets. The first pressure spike needs further study because it is suspected to be due to the numerical treatment of the splitting. However, the N-shaped pulse obtained during the formation of the jet is believed to correspond to the signal observed at the splitting in the experiment. With more segments, the jet becomes thinner, and the pressure signal becomes sharper, i.e., shorter in time and larger in magnitude.

4 Tip vortex flow fields

The tip vortex flow field used in this study is obtained from the DF_UNCLE code, which is a Reynolds Averaged Navier-Stokes (RANS) flow solver based on the Mississippi State University code UNCLE. The tip vortex flow fields are predicted for elliptic plan form hydrofoils of two different scales; the larger one with 1 m chord and 1.5 m half span, and the smaller one with 0.5 m chord and 0.75 m half span. The inflow velocity to the two hydrofoils is 2.88 m/s, which results in the Reynolds numbers, 1.44x10^6 and 2.88x10^6, for the two cases.

After obtaining the three dimensional tip vortex flow fields, they are cast into axisymmetric flow field so that the flow field can be input to the axisymmetric solver 2DYNAFS©. This is achieved by finding the tip vortex center first and taking circumferential average of the field variable around various radii from the vortex center. The locus of the tip vortex center is found by connecting the lowest pressure point on each three-dimensional grid surfaces which are roughly perpendicular to the stream direction. However, the circumferential average is taken on each plane exactly perpendicular to the inflow direction. The axisymmetric flow fields obtained by this procedure for the two Reynolds numbers are shown in Figures 6 and 7.
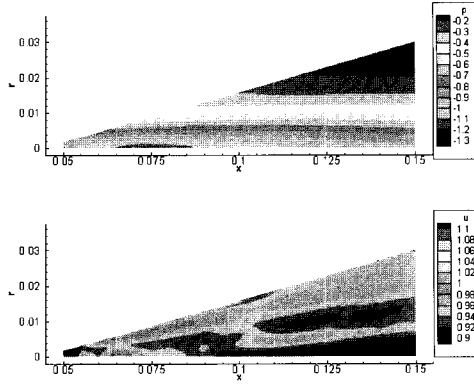
Figure 6: The axisymmetric tip vortex flow fields for Re=1.44x10⁶. Pressure field (top) and axial velocity field (bottom). The coordinates (x,r) are made dimensionless by the chord, p and u, by ρU_∞^2 and U_∞, respectively
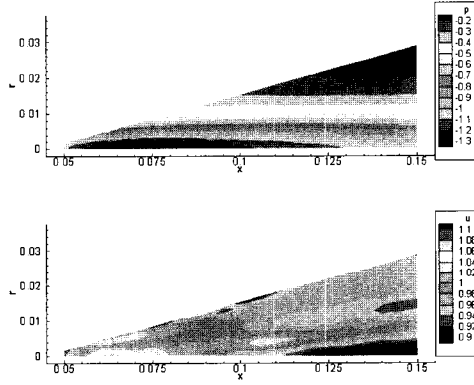

Figure 7: The axisymmetric tip vortex flow fields for Re=2.88x10⁶. Pressure field (top) and axial velocity field (bottom). The coordinates (x,r) are made dimensionless by the chord, p and u, by ρU_∞^2 and U_∞, respectively

5 Results with 50 μm bubble nucleus at Re=2.88x10⁶

In this section, the behavior of a bubble nucleus of 50 μm radius released at 0.1 m upstream of the hydrofoil tip is described. The cavitation numbers studied for this bubble nucleus range from 2.2 to 2.8. The initial pressure in the bubble nucleus is set to be in equilibrium with the ambient pressure for the corresponding cavitation number σ defined by

$$\sigma = \frac{p_\infty - p_v}{\frac{1}{2}\rho U_\infty^2} \tag{4}$$

Two representative bubble behaviors from these simulations are presented here. Figure 8 shows the final stage of the simulation for σ=2.50 when the elongated bubble finally splits and the splitted sub-bubbles develop reentrant jets. The bubble behavior at a slightly higher cavitation number, σ=2.54, in Figure 9 shows no bubble splitting but the development of a single jet from the downstream end of the elongated bubble is clearly seen.
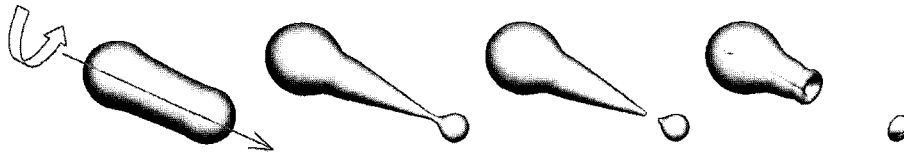
20

Figure 8: Bubble behavior at σ=2.50 as predicted by 2DYNAFS© in time sequence from top left to bottom right. The tip vortex flows from upper left to lower right as indicated by arrows
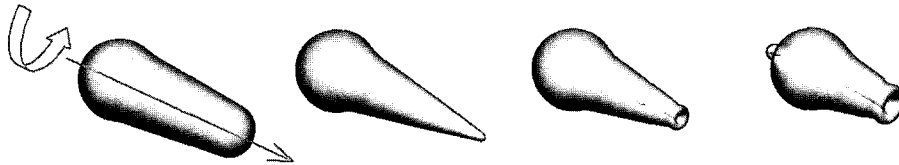

Figure 9: Bubble behavior at σ=2.54 as predicted by 2DYNAFS© in time sequence from top left to bottom right. The tip vortex flows from upper left to lower right as indicated by arrows

The bubble size can be compared between the results from the spherical model and 2DYNAFS© by representing the non-spherical bubble in 2DYNAFS© as having an equivalent bubble radius, defined as the radius of a spherical bubble of the same volume. The spherical model used in this comparison is so called the Surface Averaged Pressure (SAP) spherical model (Hsiao and Chahine 2002, Hsiao et al 2003), which gives far more accurate predictions than the classical spherical model. The time histories of the equivalent radius of the bubble are shown in Figure 10 for three selected cavitation numbers. In the two low cavitation number cases (σ=2.20 and 2.50), 2DYNAFS© results show that the bubble experiences splitting a little while after passing the maximum size. On the other hand, the result at a higher cavitation number of σ=2.54 (just below the inception which is at σ=2.57) shows the development of a single jet at the downstream end of the bubble after passing the maximum size. For all of the three cases, the SAP spherical model predicts collapse/rebound sequences with decreasing maximum radii. The general trend of decreasing maximum bubble size as the cavitation number increases can be observed in both of the predictions by SAP spherical model and 2DYNAFS©.

The maximum (equivalent) radius which a bubble ever reaches under a given cavitation number condition is presented in Figure 11 for cavitation numbers ranging from 2.2 to 2.8. Within the range below cavitation inception, the maximum equivalent radius predicted by 2DYNAFS© is larger than the maximum radius predicted by the SAP spherical model. However, both methods predict the same bubble size above the inception, and thus predict the same cavitation inception number of 2.57. Below the cavitation inception number, the maximum bubble size suddenly becomes orders of magnitude larger than the bubble size above the inception. Such a good accuracy of SAP spherical model in predicting the inception is expected because the bubble size near the cavitation inception condition is very small and the assumption of spherical bubble can be well justified for such small bubbles. The bubble size predicted by 2DYNAFS© is larger for lower cavitation numbers because the non-spherical elongation of the bubble along the vortex axis makes the bubble even larger. Interestingly, the prediction from the three dimensional method coupled
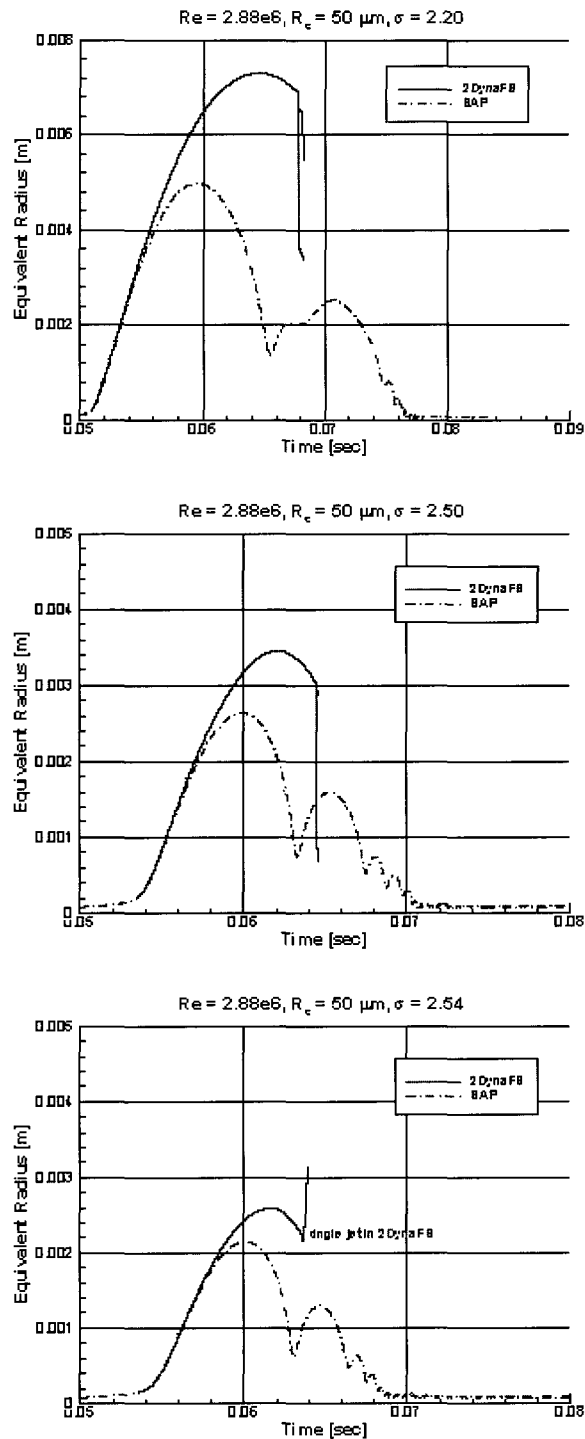
Figure 10: Equivalent radius of the bubble as it flows downstream for four different cavitation numbers, 2.20, 2.50, and 2.54. Note that the cavitation inception is predicted at σ=2.57 as shown in Figure 11
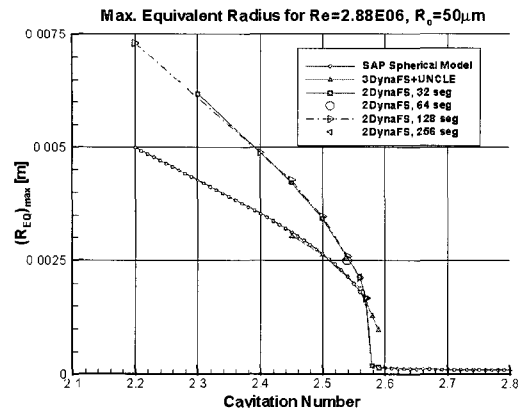
Figure 11: Comparison of the maximum (equivalent) radii between the SAP spherical model and 2DYNAFS© over the studied range of cavitation numbers. The cavitation inception based on these curves is at $\sigma=2.57$
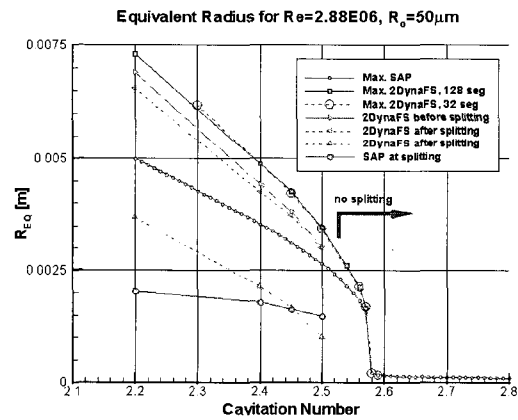

Figure 12: The equivalent radii of the bubble at the moment of splitting and the radii of the resulting sub-bubbles over the studied range of cavitation numbers

with viscous flow solver (marked as "3DynaFS + UNCLE" in the figure) is very close to the result from the SAP spherical model. This is due to the fact that the fully coupled viscous effect that makes the bubble smaller, balances with the axial elongation effect that make the bubble larger. It can be also observed in the figure that the convergence of 2DYNAFS© with respect to the number of segments is well established within the range from 32 to 256 segments.

In Figure 12, the equivalent radii of the bubbles at the moment of their splitting, those of the splitted sub-bubbles, and those predicted by the SAP spherical model at the moment of 2DY-NAFS©-predicted splitting are shown with the maximum radii each bubble has reached. The equivalent radius of the bubble at splitting is consistently smaller than the maximum equivalent radius by the amount of approximately 0.5 *mm*. The size of the larger sub-bubble after the splitting is only slightly smaller than the size of the bubble just before the splitting. This difference of the size between the bubble just before the splitting and the larger sub-bubble becomes even smaller as the cavitation number increases and approaches the inception number. When the cavitation
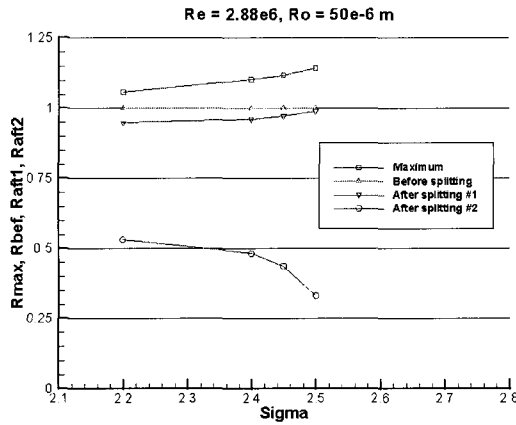
23

Figure 13: The ratios of the equivalent radii of the bubble and the sub-bubbles, relative to the equivalent radius just before the splitting
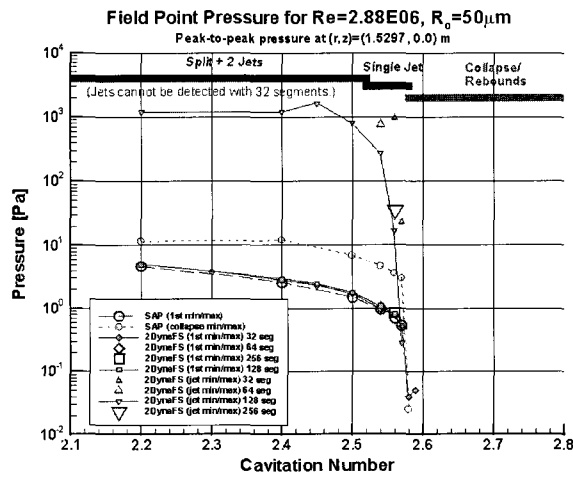

Figure 14: Pressure peaks predicted by the SAP spherical model and by 2DYNAFS©

number approaches very close to the inception, there is no smaller sub-bubble because the bubble does not split as seen in Figure 9.

In order to study the relative size of the bubbles before and after splitting, we study the ratios of the equivalent radii of the bubble before and after the splitting. The ratios among the equivalent radii relative to the equivalent radius at the moment of splitting are shown in Figure 13. The ratio of the maximum equivalent radius increases from 1.06 to 1.15 as the cavitation number increases from 2.2 to 2.5. The ratio for the larger sub-bubble just after the splitting increases from 0.95 to 0.99, while the ratio for the smaller sub-bubble decreases from 0.55 to 0.2 as the cavitation number increases from 2.2 to 2.5. These ratios become almost constant as the cavitation number decreases.

During each simulation, the pressure at a field point is computed and recorded. The field point is located 1.53 m away from the vortex center in the radial direction and at the same axial location of the tip. The field point pressure predicted by the SAP spherical model usually has
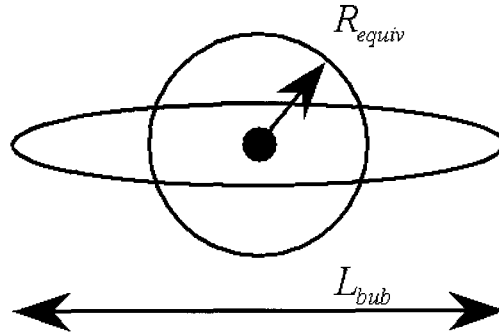
24

Figure 15: Definition of the shape factor, $L_{bub}/2R_{equiv}$

multiple peaks with the first peak near the abrupt growth of the bubble and the largest peak at the first collapse/rebound of the bubble. 2DYNAFS© usually predicts similar behavior during the initial growth but develops very higher pressure peaks when a reentrant jet is formed. The peak-to-trough values of the pressure at the field point for a range of cavitation numbers are compared in Figure 14. The first peak of pressure signal predicted by the two methods near the sudden growth of the bubble agrees very well with each other for the range of cavitation number studied. However, the maximum pressure peak values from the 2DYNAFS© prediction are about two orders of magnitude higher than the maximum predicted by the SAP spherical model. This is due to the fact that the high pressure created at the development of the jet exists only in the case of 2DYNAFS© predictions. The convergence of the predicted peak pressure with respect to the number of segments is good for the first peak predictions. The convergence for the peak pressure from the jet is also acceptable except for the smallest number of 32 segments. With 32 segments, the jet after the splitting cannot be detected, and the size of the jet is over-predicted in single jet cases. Overall the flattening trend of the curves toward the lower cavitation numbers is observed for all the pressure peaks.
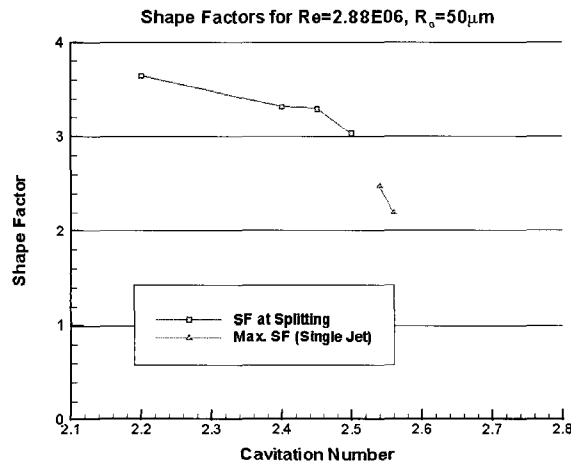

Figure 16: Shape factor as a function of cavitation number

The shape factor is defined as the ratio of the half length of the bubble along the vortex axis to the equivalent radius of the bubble as shown in Figure 15. As the bubble elongates more along the vortex axis the shape factor becomes larger and reaches its maximum just before the splitting or just before the formation of a single jet. Figure 16 shows how the maximum shape factor varies with the cavitation number. For cavitation number just below the inception, the maximum shape factor reaches 2.2 to 2.5 before the single jet start to develop. For lower cavitation numbers, the maximum shape factor which is observed just before the bubble splits ranges 3.0 to 3.6. The bubble elongates more as the cavitation number decreases.

6   Reynolds number effect

In order to observe the Reynolds number effect on the bubble size and the pressure peaks, the results in the previous section are compared with the corresponding results from the simulations using the tip vortex flow field at Reynolds number 1.44 million. The equivalent radii of the bubbles and sub-bubbles are compared in Figure 17. The cavitation inception based on the bubble radius occurs at $\sigma=2.57$ for Re=2.88×10^6, and at $\sigma=2.10$ for Re=1.44×10^6. The trend of the maximum bubble size is found to be very similar between the two Reynolds numbers. The bubbles do not split for the cavitation numbers just below the inception in both Reynolds number cases. However, the relative magnitude of the bubble size becomes smaller for the lower Reynolds number cases.
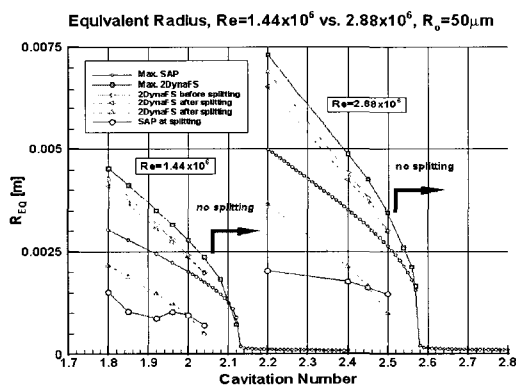

Figure 17: Comparison of the equivalent radii for two Reynolds numbers, 1.44×10^6 and 2.88×10^6

In Figure 18, the ratios of the equivalent radii are compared for the two Reynolds numbers. The ratios look similar for the two Reynolds numbers except that they are shifted by the amount of the difference in the cavitation inception numbers. For both Reynolds numbers, the radii ratio curves become flatter as the cavitation number decreases well below the cavitation inception number.

The shape factors are compared between the two Reynolds numbers in Figure 19. We observe the same shift in cavitation numbers that corresponds to the known ratio of the core size to some power between the two Reynolds number cases. The shape factors at the splitting for the lower cavitation number are observed to be about 0.4 greater than those for higher cavitation number. The threshold shape factor between the single jet and the splitting seems to increase from about 2.8 for Re=2.88×10^6 to about 3.0 for Re=1.44×10^6.
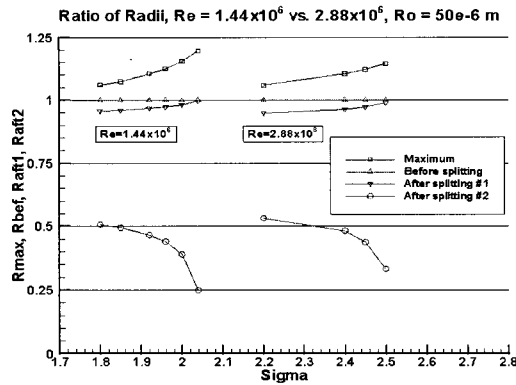
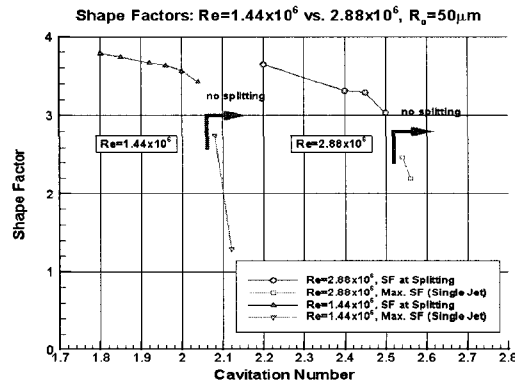**Figure 18:** Comparison of the equivalent radius ratios for two Reynolds numbers, 1.44×10^6 and 2.88×10^6

Figure 19: Comparison of the shape factors for two Reynolds numbers, 1.44×10^6 and 2.88×10^6
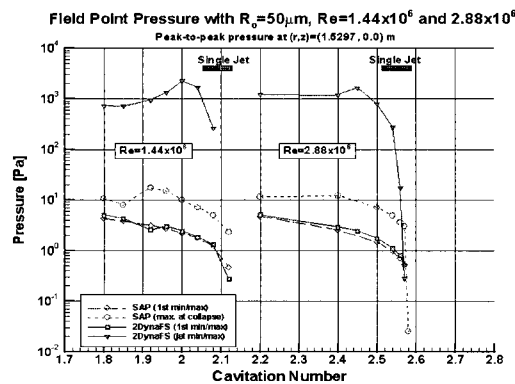

Figure 20: Comparison of the pressure signals for two Reynolds numbers, 1.44×10^6 and 2.88×10^6

The peak magnitudes of the pressure signals are compared in Figure 20. The shift of the cavitation inception number is observed between the results from the two Reynolds numbers. The peak pressure curve predicted by the SAP spherical model for Reynolds number 1.44 million has a little irregularity in the low cavitation numbers, which is due to the fact that the highest pressure is observed at the second or later collapses/rebounds rather than at the usual first one. The magnitude of the pressure does not seem to depend on the Reynolds numbers, but depends on how far the cavitation number deviates from the cavitation inception number.

7 Bubble nucleus size effect

The bubble nucleus size effect is studied by comparing results from the simulations with four different initial bubble sizes in the flow field for Re=2.88x10^6. In addition to the initial bubble radius of 50 μm, simulations with the initial radius of 10, 20, and 100 μm are conducted. The radii just before and after the splitting as well as the maximum radii from the SAP spherical model and the 2DYNAFS$^©$ are compared in Figure 21. The equivalent radii of the smaller initial bubble size
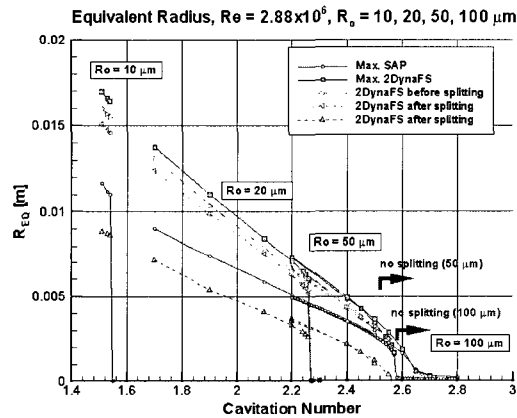

Figure 21: Comparison of the equivalent radii for four initial bubble sizes, 10, 20, 50, and 100 μm

seem to lie on the straight lines extended from the lower cavitation number portion of the radius curves for the larger initial bubble size. The threshold cavitation number between the bubble splitting and the single jet decreases as the initial bubble radius decreases from 100 μm to 50 μm. However, single jet behavior cannot be observed for the smaller initial bubble radii of 10 and 20 μm.

In Figure 22, the ratios of the equivalent radii are compared for the four initial bubble radii. The flattening trend prevails for the lower cavitation numbers regardless of the initial bubble sizes. As the cavitation number decreases, the ratio for the maximum equivalent radius approaches 1.06, the ratio for the larger sub-bubble just after the split approaches 0.95, that for the smaller sub-bubble approaches 0.55 regardless of the initial bubble sizes.

The maximum shape factors the bubbles can reach are compared in Figure 23. The maximum shape factors for all initial radii seem to follow a common slightly S-shaped curve as the cavitation number increases. A bubble with larger initial bubble size tends to split at a smaller shape factor (or at a less elongation) in higher cavitation number. A bubble with the initial radius of 100 μm
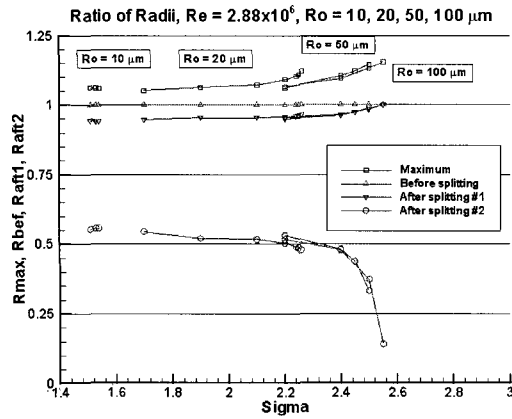
Figure 22: Comparison of the ratios of the equivalent radii for four initial bubble sizes, 10, 20, 50, and 100 μm
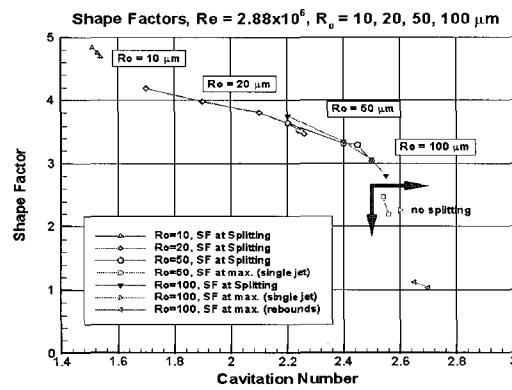

Figure 23: Comparison of the shape factors for four initial bubble sizes, 10, 20, 50, and 100 μm
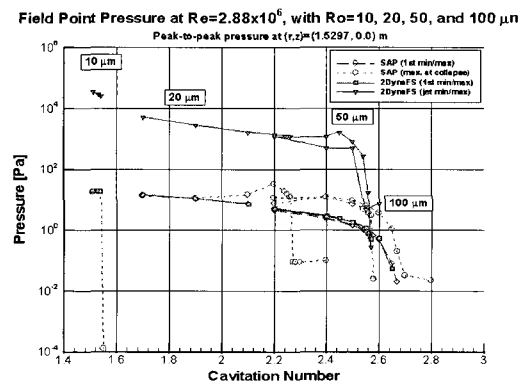

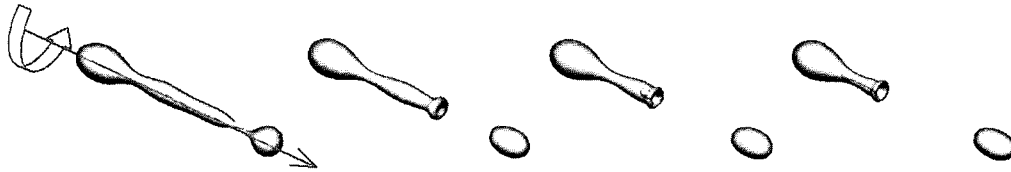**Figure 24:** Comparison of pressure signals for four initial bubble sizes, 10, 20, 50, and 100 μm

29

Figure 25: Example of a jet developing through a long tubular sub-bubble observed for $\sigma=1.51$ with a 10 μm initial bubble. Images from top left to bottom right in time sequence. The tip vortex flows from upper left to lower right

can reach the splitting at the shape factor as low as 2.8, which is the lowest limit for splitting found in this study. The single jet behavior is observed in a narrow region of the shape factors between 2.0 and 2.5, and for the cavitation numbers between 2.56 and 2.60.

The peak-to-trough values of the pressure signal peaks are compared in Figure 24. The first peak pressures predicted from SAP spherical model and 2DYNAFS© agree throughout the studied cavitation numbers. Moreover these pressure data form a common curve regardless of the initial bubble sizes. This curve of the first peak pressure flattens out as the cavitation number decreases. The maximum peak pressure predicted by SAP spherical model forms a hump just below the cavitation inception but becomes closer to the first peak pressure as the initial bubble size decreases and the cavitation number decreases. This is due to the fact that the first peak becomes the largest peak as the cavitation number and the initial bubble size decrease. The maximum pressure peaks predicted by 2DYNAFS© are always observed at the development of the jet that follows the bubble splitting. The maximum pressure peaks predicted with 50 and 100 μm show more or less similar behaviors with a small hump just below cavitation inception. This curve continues smoothly to the data obtained with 10 and 20 μm initial bubbles, curving up slightly toward the lower cavitation numbers. This might be due to the fact that the jet developed from 10 μm initial bubble is much longer (through a long tubular part of the sub-bubble) than the other jets found in larger size bubble simulations. An example of such a long jet observed for $\sigma=1.51$ is shown in Figure 25.

8 Bubble splitting model

The axisymmetric simulations using 2DYNAFS© has the advantage that non-spherical bubble behaviors, such as elongation, splitting, and reentrant jets, and the pressure signals from such behavior can be predicted. However, these simulations require more expensive computing cost than that of the simulations by the SAP spherical model. In order to perform massive simulations with multiple bubble nuclei, a simpler model is required so that the bubble splitting can be handled within the spherical model. In the new spherical model, once a bubble reaches a condition that it should split, the bubble is replaced with two spherical sub-bubbles and the simulation is continued with the new sub-bubbles. The splitting model will be more useful for cavitation numbers much lower than the inception because the bubble usually does not split near the cavitation inception. The new model should be able to answer the next two questions: (a) *Criteria of splitting:* When should a bubble split? (b) *Initial condition of the sub-bubbles:* What is the size of each sub-bubble? What is the pressure inside each sub-bubble?

From the studies described in the previous sections, a bubble splits when the shape factor

reaches a value between 2.8 and 4.8 depending on the cavitation number and the initial bubble size. Since the shape factor cannot be calculated within the spherical model, it cannot be used in the spherical model to determine if a bubble should split. However, the ratio of the maximum equivalent bubble radius relative to the equivalent radius just before the splitting can be used as a criterion. This ratio is flat at 1.05 for lower cavitation numbers and increases up to 1.15 as the cavitation number approaches the inception. In other words, the following criterion can be used to determine when a bubble should split for lower cavitation numbers.

Bubble splitting criteria for low cavitation numbers: *When the bubble radius decreases to 0.95 of the maximum after the bubble reaches its maximum radius, the bubble splits.*

Once the splitting is detected from the above criteria, the size of sub-bubbles can be determined also from the ratios shown in Figure 22. The equivalent radii of the larger and the smaller sub-bubbles are, respectively, 0.95 and 0.55 of the equivalent radius before the splitting. The gas pressure inside the sub-bubbles can be modeled with the introduction of a pressure reduction factor c_p such that the pressure after the splitting can be written as

$$p_{g,after} = c_p p_{g,before} \qquad (5)$$

In an ideal case of no energy loss through the splitting, the factor c_p should be 1.0.

The radial velocity of the sub-bubbles can be observed from each simulation such as shown in Figure 10. The slope of the equivalent radius in the figure represents the radial velocity of the bubble. Just after the split, the larger sub-bubble experience a slightly slower radial velocity (smaller slope) than that just before the split while the smaller sub-bubble has a little faster radial velocity (steeper slope) than before the split. This trend is found in most of the bubble behaviors simulated with 50 and 100 μm bubble nuclei at relatively higher cavitation numbers. However, in simulations with 10 and 20 μm bubble nuclei at relatively lower cavitation numbers, the slope just after the split tends to be close to zero for both sub-bubbles as shown in Figure 26. Therefore, zero radial velocity as the initial velocity of the sub-bubbles seems to be appropriate for the lower cavitation numbers of our interest.

The initial location of the sub-bubbles can be deduced from the shape factors. As observed from Figure 23, the shape factor at the splitting is approximately 4 for lower cavitation numbers. This means that the bubble length at the splitting is approximately 8 times the radius of the bubble. If the elongated bubble just before the splitting is assumed to be a cylinder, the radius ratio between the two sub-bubbles (0.95:0.55) can be changed to the volume ratio of 0.857:0.166, and thus the axial length ratio of the cylinder 0.84:0.16. In order to place the sub-bubbles at the center of this cylindrical segment, the center of the larger sub-bubble should be placed at 0.64 radii upstream of the pre-split bubble center and that of the smaller sub-bubble is 3.36 radii downstream from the pre-split bubble center. The initial condition of the new sub-bubbles can be summarized as follows.

Initial condition of the sub-bubbles for low cavitation numbers: *The radius of the larger and smaller sub-bubbles is, respectively, 0.95 and 0.55 of the radius just before splitting. The initial gas pressure is determined from (5), and the initial radial velocity is zero. The initial location of the larger sub-bubbles is 0.64 radii upstream of the pre-split bubble center and that of the smaller one is 3.36 radii downstream of the pre-split bubble center.*
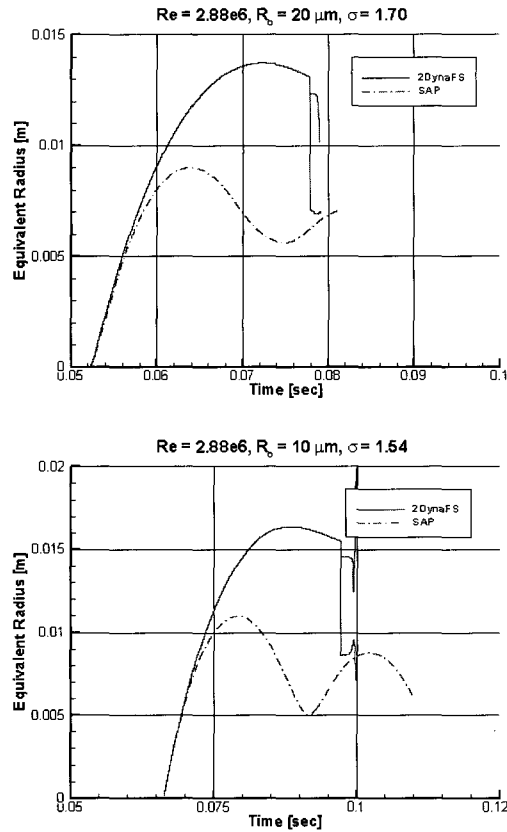
Re = 2.88e6, R_b = 20 µm, σ = 1.70

Re = 2.88e6, R_b = 10 µm, σ = 1.54

Figure 26: Equivalent radius of the bubble as a function of time predicted with 20 µm nucleus at σ=1.70 (top) and with 10 µm nucleus at σ=1.54 (bottom)

It should be noted that above model is specific to the tip vortex flow fields we have studied. However, the model covers a wide range of cavitation numbers lower than the inception and the bubble nucleus sizes between 10 and 100 µm. Efforts to expand and apply the model are currently underway.

9 Conclusion

The bubble behaviors in two tip vortex flow fields of Reynolds number 1.44 million and 2.88 million are studied by using the SAP spherical model and 2DYNAFS©, a non-spherical free surface flow solver. The equivalent radius of the non-spherical bubble and the radius predicted by the spherical model are compared in a wide range of cavitation numbers varying from 1.5 to 2.8. In addition, the peak values of the pressure signals detected from the bubble collapse/rebound and from the formation of a jet or jets are compared.

The effect of the Reynolds number is found to be mainly a shifting of the cavitation inception number both in the maximum bubble size curves and in the maximum pressure curves. The effect of initial bubble nucleus size is found to be such that, if observed from lower to higher cavitation numbers, a smaller initial bubble nucleus brings an abrupt transition to a non-cavitating status

from the common curves of the radii or of the pressure peaks at a lower cavitation number. These common curves seem to be independent of the nucleus size within the range of 10 to 100 μm for Reynolds number 2.88 million.

Through the observation of the ratios among the equivalent radii of their maximum, before and after splitting, a simple model for the bubble splitting is suggested for lower cavitation numbers. This model is based on the ratios of the equivalent radii of the bubble and sub-bubbles and the shape factors. Efforts to expand and apply the suggested model are currently underway.

Acknowledgements

References

CHAHINE, G.L. 1982 Experimental and asymptotic study of nonspherical bubble collapse. Applied Scientific Research, **38**, pp. 187-197

CHAHINE, G.L. 1995 Fluid Vortices, S. Green (ed.), Kluwer Academic, Chapter 18

CHAHINE, G.L., DURAISWAMI, R., AND KALUMUCK, K.H. 1996 Boundary element method for calculating 2-D and 3-D underwater explosion bubble loading on nearby structures including fluid structure interaction effects. Technical Report NSWC-DD/TR-93/46, Dynaflow, Inc.

CHAHINE, G.L., SARKAR, K., AND DURAISWAMI, R. 1997 Strong bubble/flow interaction and cavitation inception. Technical Report 94003-1ONR, Dynaflow, Inc.

CHOI, J.-K. AND CHAHINE, G.L. 2002 Non-spherical bubble behavior in vortex flow fields. IABEM 2002, Int. Assoc. for Boundary Element Methods, Austin, TX, May 28-30

CHOI, J.-K. AND CHAHINE, G.L. 2003 Noise due to extreme bubble deformation near inception of tip vortex cavitation. Proc. FEDSM'03, International Symposium on Cavitation Inception, 4th ASME/JSME Joint Fluids Engineering Conference, Honolulu, Hawaii, July 6-10

ISHIDA, H., NUNTADUSIT, C., KIMOTO, H., NAKAGAWA, T., AND YAMAMOTO, T. 2001 Cavitation bubble behavior near solid boundaries. Proc. CAV2001, 4th International Symposium on Cavitation, session A3, California Inst. of Tech., Pasadena, CA.

KUCHERENKO, V.V. AND SHAMKO, V.V. 1986 Dynamics of electric-explosion cavities between two solid parallel walls. J. of Applied Mechanics and Technical Physics, **27**, pp. 112-115

HSIAO, C.-T. AND CHAHINE, G.L. 2002 Prediction of vortex cavitation inception using coupled spherical and non-spherical models. Proc. 24th Symposium on Naval Hydrodynamics, ONR, Fukuoka, Japan, July 8-13

HSIAO, C.-T., CHAHINE G.L., AND LIU, H. 2003 Scaling effects on prediction of cavitation inception in a line vortex flow. J. of Fluids Engineering, **125**, pp. 53-60